AIAA JOURNAL
Vol. 54, No. 3, March 2016

Weak-Shock Interactions with Transonic Laminar Mixing Layers of Fuels for High-Speed Propulsion

César Huete*
University of California, San Diego, La Jolla, California 92093-0411
Javier Urzay†
Stanford University, Stanford, California 94305-3024
and
Antonio L. Sánchez‡ and Forman A. Williams§
University of California, San Diego, La Jolla, California 92093-0411

DOI: 10.2514/1.J054419

This paper extends to transonic mixing layers an analysis of Lighthill ("Reflection at a Laminar Boundary Layer of a Weak Steady Disturbance to a Supersonic Stream, Neglecting Viscosity and Heat Conduction," *Quarterly Journal of Mechanics and Applied Mathematics*, Vol. 54, No. 1, 1950, pp. 303–325.) on the interaction between weak shocks and laminar boundary layers. As in that work, the analysis is carried out under linear-inviscid assumptions for the perturbation field, with streamwise changes of the base flow neglected, as is appropriate given the slenderness of the mixing-layer flow. The steady-disturbance profile is determined by taking a Fourier transform along the longitudinal coordinate. Closed-form analytical functions for the pressure field are derived in the small- and large-wave-number limits, and vorticity disturbances are obtained as functions of the pressure perturbations. The analysis is particularized to ethylene–air and hydrogen–air mixing layers, for which the dynamics are of current interest for hypersonic propulsion. The results provide, in particular, the effective distance of upstream influence of the pressure perturbation in the subsonic stream. The resulting value, which scales with the thickness of the subsonic layer, is much smaller than the upstream influence distances encountered in boundary layers. This study may serve as a basis to understand shock-induced autoignition and flameholding phenomena in simplified versions of non-premixed supersonic-combustion problems.

Nomenclature

C_p	=	normalized specific heat
D	=	normalized binary diffusion coefficient
f_1, F_1	=	physical- and Fourier-space incident pressure perturbation
g_1, G_1	=	physical- and Fourier-space reflected pressure perturbation
J	=	normalized fuel-diffusion flux
k	=	normalized streamwise wave number
L, ℓ_m	=	mixing-layer development distance and thickness
Le	=	fuel Lewis number
M	=	Mach number
Pr	=	Prandtl number
$p, \mathcal{P}$	=	physical- and Fourier-space pressure perturbations
R	=	normalized density
Re	=	Reynolds number
T	=	normalized temperature
U, V	=	normalized streamwise and transverse velocities
u, v	=	normalized streamwise and transverse velocity perturbations
W	=	normalized mean molecular weight
X, Z	=	streamwise and transverse global coordinates
x, z	=	normalized streamwise and transverse local coordinates
$Y, y, \mathcal{Y}$	=	base-flow, perturbation, and Fourier- transformed fuel mass fractions
α	=	thermal-diffusion factor
β	=	cotangent of Mach angle
γ	=	ratio of specific heats
ϵ	=	normalized perturbation amplitude
η	=	self-similar variable
Θ, θ	=	physical- and Fourier-space temperature perturbations
μ	=	normalized mean viscosity
Ω	=	vorticity production factor
ω, ϖ	=	physical- and Fourier-space vorticity perturbations

Subscripts

1	=	supersonic airstream
2	=	subsonic fuel stream

Superscript

$'$	=	dimensional variables

Received 29 April 2015; revision received 10 September 2015; accepted for publication 15 September 2015; published online 7 January 2016.

*Postdoctoral Researcher, Department of Mechanical and Aerospace Engineering; chuete@ing.uc3m.es.
†Engineering Research Associate, Center for Turbulence Research.
‡Professor, Department of Mechanical and Aerospace Engineering.
§Professor, Department of Mechanical and Aerospace Engineering. Fellow AIAA.

I. Introduction

MIXING layers and shock waves are two different phenomena that coexist in hypersonic and supersonic propulsion devices. For instance, in supersonic-combustion ramjets (scramjets), shock waves are typically generated ahead of the combustion zone, where the supersonic incoming flow enters a converging nozzle and interacts with wedged walls and fuel injectors. Along its path through the combustor, the flow is subject to complex shock trains and expansion waves [1].

In scramjets, shock waves can interact with the flow in many different ways. For instance, shocks may disturb the flow near the walls, leading to sudden transition to turbulence and augmented wall heating in boundary layers. The corresponding shock/boundary-layer interaction problem is one of high practical relevance that has received a large amount of attention in recent years [2–5]. A relatively less known interaction occurs when shocks impinge on chemically

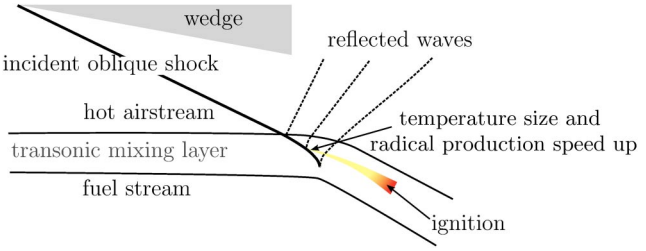

Fig. 1 Sketch of the general configuration.

reacting mixing layers of the fuel and oxidizer. To illustrate the relevance of shock/mixing-layer interaction phenomena, consider the following standard fuel-injection configurations employed in scramjets. In one configuration, the shock waves interact with the mixing layer that separates the supersonic incoming hot airstream and the subsonic fuel flow, and which is generated downstream from a strut fuel injector (see figures 5 and 11 in [6]). Similarly, in configurations with jet-in-crossflow fuel injection, a reflected bow shock interacts with the mixing layer generated from the aerodynamics of the fuel jet as it flows into the supersonic incoming hot airstream (see, for instance, figure 4 in [7]). In all cases, since the residence time of the reactants in the combustor is short in supersonic regimes, ignition typically cannot be achieved by relying on diffusion and heat conduction alone. Shock waves may help, however, to heat the mixture and speed up the mixing process: with the former arising from the inherent temperature rise across the shock wave, and the latter associated with the interaction of the shock with the nonuniform flow [5–18].

Although the aerodynamic interactions described previously are predominantly encountered in highly turbulent flows in practical applications, analytical solutions to related simplified laminar problems can be advantageous in studying such supersonic-combustion processes, helping to clarify the real configuration, not only for increasing understanding but also for suggesting scaling concepts that may prove useful in formulating subgrid-scale models. The present work, which is of that type, pertains to transonic laminar mixing layers formed by fuels employed in supersonic combustion and subjected to impingement by a shock from the airstream, roughly as illustrated in Fig. 1. As a first step, an inert mixing layer is considered, and the shocks are assumed to be sufficiently weak to be treated as linear perturbations of the base flow, with the nonlinear influences of finite-amplitude shocks on combustion and the effects of heat release being deferred to later investigations. A crucial asset for the present investigation is the earlier work by Lighthill [19,20], which was instrumental in understanding the fundamental dynamics of weak-shock impingement on wall boundary layers. Initially presented in a physical context, it was later shown by Stewartson and Williams [21] that this type of problem, involving linear (weak-shock) perturbations of a laminar viscous region at large values of the Reynolds number Re could be treated rigorously through matched asymptotic expansions for a Reynolds number approaching infinity, resulting in a triple-deck theory. This has been explained carefully in more recent reviews, such as that of Nayfeh [22], where the relationships to other triple-deck problems are made clear. The mixing-layer problem to be addressed here turns out to be a particularly simple version of multiscale problems of this type, for example, because it is unnecessary to deal with the bottom (low-speed, viscous, incompressible) deck.

The objective of this study is to describe, by using asymptotic analysis, the effect of a weak shock on an inert laminar transonic mixing layer. Particular attention is given to the effect of the perturbations in the nonslender interaction region found around the impingement point, giving a problem that can be treated using Lighthill's theory on shock/boundary-layer interaction [19,20]. Molecular-transport effects, which determine the slow evolution of the mixing-layer flow upstream from the impingement location, have, however, a negligible effect on the perturbations in the interaction region because the local Reynolds number there is large. Correspondingly, since the streamwise extent of the interaction region, of the order of the mixing-layer thickness, is much smaller than the mixing-layer development length, the streamwise variations of the background flow variables can be neglected when writing the linearized problem for the perturbations induced by the weak shock. Therefore, for the base flow only, transverse changes in the density and velocity are considered, whereas the background pressure field is assumed to be constant along and across the mixing layer in the first approximation. These approximations engender analytic solutions.

The paper is structured as follows: The background laminar mixing layer and the asymptotic perturbation theory are formulated in Sec. II. The perturbation pressure field is analyzed by means of a Fourier transformation along the streamwise direction. An ordinary differential equation for the pressure perturbations, as functions of the transverse variable, is obtained. The asymptotic results for high-frequency and low-frequency disturbances as functions of the transverse coordinate and the frequency are provided in Sec. III, followed in Sec. IV by an analysis of the upstream decay of the disturbance. Although the general analysis will be performed for a weak pressure perturbation of arbitrary shape, the specific interaction with a weak step-pressure wave, emulating the weak shock, is addressed in Sec. V, where the pressure-perturbation distribution throughout the mixing layer is computed and analyzed. The effects that the weak shock causes on the vorticity field are analyzed separately in Sec. VI. Finally, the conclusions are summarized in Sec. VII.

It is relevant to point out that there are three previous investigations of interactions of oblique shocks with mixing regions, although the specific transonic problems addressed here have not been treated. Riley [23] employed the same methods adopted here to analyze the interaction of a shock from a supersonic stream, incident at a fixed plane on a shear layer of infinite extent, in which the Mach number approached zero at infinity. Although he did not consider the mixing-layer composition and temperature profiles, such as those that we analyze, instead studying influences of two model transverse distributions of the Mach number, a number of the results of his theory are the same as ours. Moeckel [24] derived a simplified method for describing shock shapes in purely supersonic mixing regions. The same method was employed later by Buttsworth [25], who attempted computations of vorticity fields in mixing layers of ideal gases with similar and different thermodynamic properties, with his investigation being motivated by the same supersonic-combustion applications that led to our study. All of these excellent contributions explain methods, not investigated here, for taking into account influences of finite amplitudes of the incident waves.

II. Problem Formulation

We consider the interaction of a steady transonic mixing layer (separating a supersonic airstream from a subsonic fuel stream) with a small, external, steady, pressure perturbation approaching from the supersonic side. The mixing layer develops downstream from a separating splitter plate, with the perturbation reaching the mixing layer at a downstream distance of $X = L$, as indicated in Fig. 2. The distribution of flow properties across the laminar mixing layer depends on the type of air–fuel mixture, with two different relevant cases considered in the following. A first set of integrations neglects variations of the mean molecular weight and assumes a unity Lewis number when describing the fuel-diffusion velocity, with thermal diffusion neglected. This simplified case is representative of fuels that have properties close to those of air, such as ethylene, which has been employed in recent supersonic-combustion research [26]. The properties of ethylene [27] are not exactly those of air but, as will be shown, they are sufficiently close for its behavior to be approximated well by that of the simplified case. Investigation of hydrogen, also a promising candidate for high-speed combustion because of its favorable chemical properties (high mass-based energy density and high reactivity), requires a separate analysis including consideration of its specific physical properties, i.e., low molecular weight, high diffusivity, and nonnegligible thermal diffusion.

The relevant Reynolds number of the flow $Re = \rho_1' U_1' L/\mu_1'$, based on the velocity U_1', density ρ_1', and shear viscosity μ_1' of the supersonic stream, is assumed to be moderately large and comparable in magnitude to the corresponding value $\rho_2' U_2 L/\mu_2'$ based on the subsonic-stream properties. This results in a slender mixing layer, for which the characteristic thickness increases according to

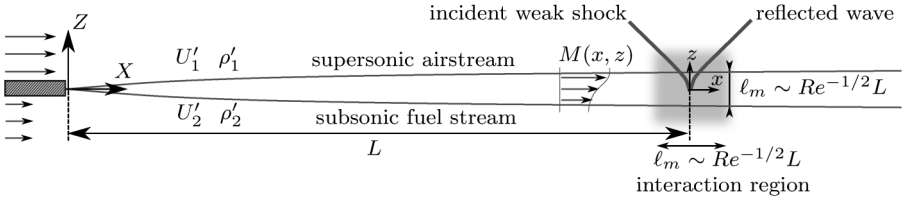

Fig. 2 Sketch of the model problem.

$[(\mu'_1/\rho'_1)X/U_1]^{1/2}$, reaching a value ℓ_m of order $Re^{-1/2}L \ll L$ at $X = L$. Since the relative magnitude of the external pressure perturbation ϵ is assumed to be infinitesimally small, in the first approximation, the flow variables are given by those of the unperturbed laminar mixing layer, which is known to possess a self-similar solution, to be described in Sec. II.A. The interaction of the perturbation with the mixing layer occurs in a nonslender region of characteristic size ℓ_m, where the relevant local Reynolds number is $\rho'_1 U'_1 \ell_m/\mu'_1 \sim Re^{1/2} \gg 1$. In the double limit $Re \gg 1$ and $\epsilon \ll 1$, the interaction region can be analyzed following Lighthill's seminal work [19,20], by linearizing the conservation equations around the background solution, with molecular-transport terms neglected at the leading order, along with the small streamwise variations of the base flow, of order $Re^{-1/2}$ for the slender mixing layer considered here.

A. Transonic Mixing Layer

In the absence of external perturbations, the transonic mixing layer that develops downstream from the splitter plate possesses a self-similar solution in terms of the rescaled transverse coordinate $\eta = Z/[(\mu'_1/\rho'_1)X/U'_1]^{1/2}$. In the description, the longitudinal and transverse velocity components are scaled with their characteristic values U'_1 and $[(\mu'_1/\rho'_1)U'_1/X]^{1/2}$ to define the nondimensional functions $U(\eta)$ and $V(\eta)$, whereas the temperature and density are scaled with their air-side values T'_1 and ρ'_1, respectively, to define $T(\eta)$ and $R(\eta)$. The adiabatic pressure disturbances in the interaction region will be found in the following to be governed by an equation that depends only on the distribution of the Mach number $M(\eta)$ across the mixing layer. Since the ratio γ of specific heats is essentially constant in these ideal-gas mixtures, the sound speed is inversely proportional to the square root of the density because the pressure does not vary appreciably across the mixing layer. As a result, the distribution of Mach number $M(\eta)$ can be evaluated from the nondimensional velocity and density profiles according to

$$M(\eta) = M_1 U(\eta) R(\eta)^{1/2} \tag{1}$$

where $M_1 > 1$ is the Mach number of the airstream, yielding the relation $M_2 = M_1 U_2 R_2^{1/2} < 1$ for the fuel stream Mach number.

Since nitrogen and oxygen are very similar, they will be treated in the following as a single species, thereby reducing the mixing process to that of a binary mixture, with the local composition characterized in terms of the fuel mass fraction Y. The corresponding fuel-diffusion flux, nondimensionalized with $[\rho'_1\mu'_1 U'_1/X]^{1/2}$, can be shown to be expressible in the explicit form [28]

$$J = -\frac{RD}{PrLe}\left(\frac{\mathrm{d}Y}{\mathrm{d}\eta} + \alpha\frac{Y(1-Y)}{T}\frac{\mathrm{d}T}{\mathrm{d}\eta}\right) \tag{2}$$

accounting for both species gradient diffusion and thermal diffusion. The latter, known as the Ludwig–Soret effect, exerts significant influences in laminar hydrogen–air mixing layers, whereas its reciprocal Onsager property, known as the Dufour effect, has little influence on the results. Here, $Pr = \mu' c_p/\lambda$ is the Prandtl number of the gas mixture, assumed here to be constant and equal to $Pr = 0.7$, with λ and c_p representing the thermal conductivity and the specific heat at constant pressure of the mixture. The ratio of the thermal diffusivity $\lambda/(\rho' c_p)$ to the fuel–air binary diffusion coefficient D' is the Lewis number, which is a quantity that depends on the mixture composition through the variation of $\lambda/(\rho' c_p)$ with molecular weight. Its value in the airstream $Le = \lambda_1/(\rho'_1 c_{p1} D'_1)$ appears to be multiplying the Prandtl number in Eq. (2), which includes the dimensionless binary diffusion coefficient $D = D'/D'_1$, which is a function of the temperature given in Eq. (8). The thermal-diffusion factor α [the ratio of the thermal-diffusion coefficient to the product $Y(1-Y)\rho' D'$] will be taken to be constant, which is a sufficiently accurate approximation for hydrogen–air mixtures, for which $\alpha \simeq -0.3$ [28].

In terms of the aforementioned dimensionless variables, the conservation equations can be written in the boundary-layer form

$$-\frac{\eta}{2}\frac{\mathrm{d}}{\mathrm{d}\eta}(RU) + \frac{\mathrm{d}}{\mathrm{d}\eta}(RV) = 0 \tag{3}$$

$$R\left(V - \frac{\eta}{2}U\right)\frac{\mathrm{d}U}{\mathrm{d}\eta} = \frac{\mathrm{d}}{\mathrm{d}\eta}\left(\mu\frac{\mathrm{d}U}{\mathrm{d}\eta}\right) \tag{4}$$

$$\begin{aligned} RC_p\left(V - \frac{\eta}{2}U\right)\frac{\mathrm{d}T}{\mathrm{d}\eta} &= \frac{\mathrm{d}}{\mathrm{d}\eta}\left(\frac{\mu C_p}{Pr}\frac{\mathrm{d}T}{\mathrm{d}\eta}\right) - (W_2^{-1} - 1)J\frac{\mathrm{d}T}{\mathrm{d}\eta} \\ &\quad - \frac{\alpha(\gamma-1)}{W_2\gamma}\frac{\mathrm{d}}{\mathrm{d}\eta}(WJT) + (\gamma-1)M_1^2\mu\left(\frac{\mathrm{d}U}{\mathrm{d}\eta}\right)^2 \end{aligned} \tag{5}$$

$$R\left(V - \frac{\eta}{2}U\right)\frac{\mathrm{d}Y}{\mathrm{d}\eta} = -\frac{\mathrm{d}J}{\mathrm{d}\eta} \tag{6}$$

where $\mu = \mu'/\mu'_1$, $C_p = c_p/c_{p1}$, and $W = W'/W'_1$ (W' denoting molecular weights) are the shear viscosity, specific heat, and mean molecular weight scaled with their airstream values, respectively; and $W_2 = W'_2/W'_1$.

The preceding equations must be supplemented with the equation of state

$$RT = W = \frac{1}{1 + (W_2^{-1} - 1)Y} \tag{7}$$

and with the expressions

$$\begin{aligned} &\mu = \frac{1 + [(\mu'_2/\mu'_1)W_2^{-1/2} - 1]Y}{1 + (W_2^{-1/2} - 1)Y}T^{\sigma_1}, \quad D = T^{1+\sigma_1}, \quad \text{and} \\ &C_p = [1 + (W_2^{-1} - 1)Y]T^{\sigma_2} \end{aligned} \tag{8}$$

for the variation with temperature and composition of the transport coefficients and specific heat. The representative values $\sigma_1 = 0.7$ and $\sigma_2 = 0.2$ are used in the following for the temperature exponents. The semiempiric expression used for the viscosity of a binary mixture, taken from [29], and that employed for C_p, which follows from assuming that the molar specific heat at constant pressure is identical for the fuel and the air, are approximate descriptions that give excellent accuracy in many configurations of interest: notably for hydrogen–air mixtures. The temperature variations in Eq. (8) and the assumption that the Prandtl number $Pr = \mu' c_p/\lambda$ is constant are consistent with a Lewis number $\lambda/(\rho' c_p D')$ that has a negligible temperature dependence and a thermal conductivity that increases

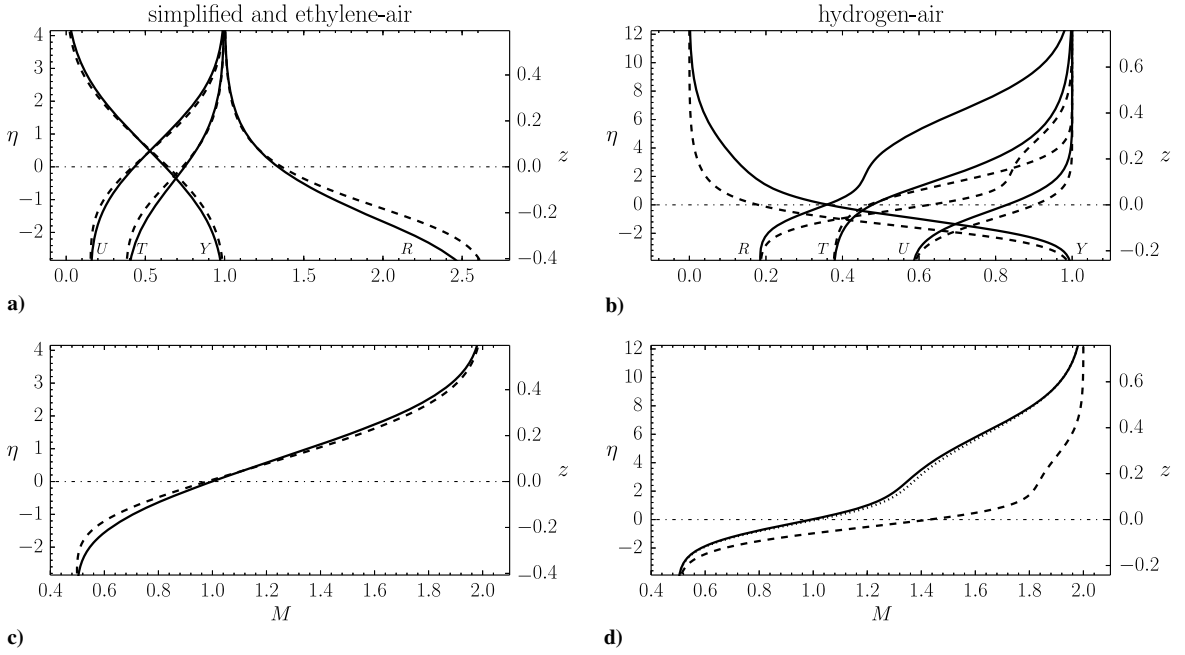

Fig. 3 Profiles of U, T, R, Y, and M for simplified and ethylene–air mixing layers and for a hydrogen–air mixing layer with $T_2 = 0.375$, $M_1 = 2$, and $M_2 = 0.5$.

with temperature according to $\lambda \propto T^{\sigma_1+\sigma_2}$. In the simplified case that approximates ethylene as the fuel, the dependences on Y disappear from Eqs. (7) and (8), with $W = W_2 = 1$ and $\mu_2' = \mu_1'$, giving $\mu = 1$, $C_p = 1$, and, in Eq. (2), $J = T^{\sigma_1}(\mathrm{d}Y/\mathrm{d}\eta)/Pr$.

The problem reduces to the integration of Eqs. (3–6) supplemented with Eqs. (7) and (8) and subject to the boundary conditions $U = 1$, $T = 1$, and $Y = 0$ as $\eta \to \infty$ and $U = U_2$, $T = T_2$, and $Y = 1$ as $\eta \to -\infty$, together with the additional boundary condition $M = M_1 UR^{1/2} = 1$ at $\eta = 0$, stating that the arbitrary origin of the transverse coordinate η is selected to be the sonic point. The resulting description is similar to that presented in a previous analysis of transient hydrogen–air mixing [30]. A distinguishing feature of the present analysis is the inclusion of the last two terms in Eq. (5), which represent, respectively, the Dufour effect, by which an energy flux is generated by gradients of species concentrations and the heating by viscous dissipation, which is relevant for the transonic conditions examined here. Integrations were performed for fuel streams composed of hydrogen ($Le = 0.3$, $\alpha = -0.3$, $W_2 = 0.069$, and $\mu_2' = 0.514\mu_1'$) and ethylene ($Le = 1.2$, $W_2 = 0.97$, and $\mu_2' = 0.6\mu_1'$ [27]). Additionally, comparisons were made between ethylene–air and air–air mixing layers (with $Le = 1, \alpha = 0, W_2 = 1$, and $\mu_2' = \mu_1'$ employed for air), which showed that both configurations yielded qualitatively similar results. Sample profiles of U, T, R, and Y obtained for the case $T_2 = 0.375$ with $M_1 = 2$ and $M_2 = 0.5$ are shown in Fig. 3, which also displays the corresponding distributions of Mach number, evaluated from Eq. (1).

The results shown in Figs. 3a and 3c appear quite symmetric, whereas those for hydrogen–air systems are more irregular, exhibiting, for example, three inflection points in the profiles of density and Mach number. These differences are due to the specific properties of hydrogen: notably, its low molecular weight and high diffusivity. Thus, for both the ethylene–air and simplified cases, in which the molecular-weight variation is unimportant, the density decreases as the temperature increases across the mixing layer from the subsonic to the supersonic stream, i.e., such that $\mathrm{d}R/\mathrm{d}z < 0$ everywhere. For the hydrogen–air mixing layer, however, the density changes associated with molecular weight variations are sufficiently large that, for the air-to-fuel temperature ratio selected in the figure, the corresponding density profile becomes an increasing function of z. These differences in transverse density gradient will be seen later to have a significant effect on the vorticity generated by baroclinic torque.

The larger thickness of the hydrogen–air mixing layer, seen from the different scales in the left and right columns of Figs. 3b–3d, is a direct consequence of the higher molecular diffusivity of the H_2 molecules, which is apparent in their small Lewis number $Le = 0.3$, and of the augmented transport rate associated with thermal diffusion. The latter phenomenon is seen to have a prominent effect on the solution, as was verified by performing calculations with $\alpha = 0$, giving the profiles represented by the dashed curves in Fig. 3b. The modifications in the hydrogen distribution are seen to alter significantly the profiles of the other flow variables, especially those of density and Mach number. In particular, as can be inferred from the resulting $M(\eta)$, in the absence of thermal diffusion, the supersonic boundary of the mixing layer would be much closer to the sonic plane. Also of interest is that the Dufour effect comparatively has a much smaller influence on the solution, as revealed by the dotted Mach number profile in Fig. 3d, obtained by selectively removing the Dufour term in the energy equation [i.e., setting $\alpha = 0$ in Eq. (5)]. Thermal diffusion is therefore important only through the Soret effect in this problem, as is often the case.

The sonic conditions, denoted by the superscript $*$, are reached at $\eta = 0$. At this point, the nondimensional temperature and fuel mass fraction are $T^* = 0.71$ and $Y^* = 0.65$ for the simplified case and $T^* = 0.48$ and $Y^* = 0.36$ for hydrogen–air mixing layers. Since the shock penetration will be seen to terminate at the sonic point, it is thus found to end closer to the properties of the fuel stream in the simplified case than in the hydrogen–air layer. Largely because of the high sound speed of hydrogen, however, the resulting distance from the sonic point to the subsonic boundary, measured relative to the total mixing-layer thickness, turns out to be considerably smaller in hydrogen–air mixing layers when the Mach numbers of the streams are fixed. This specific characteristic of the mixing-layer structure will be seen to have an effect on the rate of decay of the acoustic disturbances. With regard to the fuel-mass-fraction profiles, it is also worth noting that the stoichiometric value is always a very small quantity (e.g., $Y_{st} = 0.063$ and $Y_{st} = 0.028$ for ethylene–air and hydrogen–air mixtures, respectively), so that the most favorable mixing conditions for ignition are always found near the air supersonic stream.

The self-similar profiles can be used to evaluate the thickness of the mixing layer. Different definitions are appropriate for different applications. Since the interactions investigated in the following depend fundamentally on the Mach number distribution, it seems

appropriate to use the condition of achievement of 99% of the freestream Mach number as the defining criterion for the location of the upper and lower edges of the mixing layer η_1 and η_2, giving, for instance, $\eta_1 = 4.15$ and $\eta_2 = -2.85$ for the ethylene–air case and $\eta_1 = 12.25$ and $\eta_2 = -3.9$ for the hydrogen–air mixing layer shown in Fig. 3. Correspondingly, the analysis yields the value

$$\ell_m = (\eta_1 - \eta_2)[(\mu_1'/\rho_1')L/U_1']^{1/2} \tag{9}$$

for the mixing-layer thickness at $X = L$, to be used in the following as a scale for the interaction region. Because of the initial factor in this equation, for the conditions of Fig. 3, the hydrogen–air mixing layer is more than twice as thick as the ethylene–air layer. The convective Mach number, although most commonly employed for turbulent mixing layers, is also known to be readily definable for laminar mixing layers [31], namely,

$$M_c = \frac{U_1' - U_2'}{[(\gamma-1)c_{p_1}T_1']^{1/2} + [(\gamma-1)c_{p_2}T_2']^{1/2}} = M_1\frac{1-U_2}{1+R_2^{-1/2}} \tag{10}$$

which yields 1.05 for the ethylene–air case but only 0.25 for hydrogen–air. This trend is similar to the general one found in turbulent mixing layers, in that mixing-layer thicknesses decrease with increasing convective Mach numbers [32].

B. Perturbed Pressure Field

The interactions of the external pressure perturbation with the mixing layer will be studied in a reference frame for which the origin is placed at the intersection of the incident wave with the sonic line, located at $(X, Z) = (L, Z^*)$. Using ℓ_m as the characteristic length results in the local coordinates $x = (X - L)/\ell_m$ and $z = (Z - Z^*)/\ell_m$. In the interaction region, the streamwise variations of the velocity, density, temperature, and fuel mass fraction of the unperturbed base flow are small, on the order of $Re^{-1/2}$, and they can therefore be neglected in the first approximation, along with the departures of the base-flow pressure from the ambient value p_o' of order Re^{-1}. The external pressure perturbation introduced is assumed to be of order $\epsilon p_o'$, leading to relative departures from the base flow of order ϵ given by

$$\frac{u'}{U_1'} = U(z) + \epsilon u(x,z), \qquad \frac{v'}{U_1'} = Re^{-1/2}V(z) + \epsilon v(x,z),$$
$$\frac{\rho'}{\rho_1'} = R(z) + \epsilon\rho(x,z), \qquad \frac{p'-p_o'}{\gamma p_o'} = \epsilon p(x,z) \tag{11}$$

where the base profiles $U(z)$, $V(z)$, and $R(z)$ can be evaluated from the self-similar profiles $U(\eta)$, $V(\eta)$, and $R(\eta)$ with use made of $z = \eta/(\eta_1 - \eta_2)$. The normalized transverse coordinate z is included for completeness in the plots of Figs. 3a–3d. Note that, with the scaling introduced, the edges of the mixing layer $z_1 = \eta_1/(\eta_1 - \eta_2)$ and $z_2 = \eta_2/(\eta_1 - \eta_2)$ are such that $z_1 - z_2 = 1$.

Since the local Reynolds number in the interaction region $\rho_1' U_1' \ell_m/\mu_1'$ is large, on the order of $Re^{1/2} \gg 1$, the perturbations are governed by the Euler equations, which can be linearized about the base-flow solution to give

$$R\frac{\partial u}{\partial x} + U\frac{\partial \rho}{\partial x} + v\frac{\mathrm{d}R}{\mathrm{d}z} + R\frac{\partial v}{\partial z} = 0 \tag{12a}$$

$$RU\frac{\partial u}{\partial x} + Rv\frac{\mathrm{d}U}{\mathrm{d}z} + \frac{1}{M_1^2}\frac{\partial p}{\partial x} = 0 \tag{12b}$$

$$RU\frac{\partial v}{\partial x} + \frac{1}{M_1^2}\frac{\partial p}{\partial z} = 0 \tag{12c}$$

$$U\frac{\partial p}{\partial x} = \frac{U}{R}\frac{\partial \rho}{\partial x} + \frac{v}{R}\frac{\mathrm{d}R}{\mathrm{d}z} \tag{12d}$$

with the last expressing the conservation of entropy along any given streamline. The fuel mass fraction and the temperature are also modified by the external pressure perturbation, giving departures that can be described by introducing $Y(z) + \epsilon y(x,z)$ and $T(z) + \epsilon\theta(x,z)$. The perturbation to the mass fraction field, resulting from the deflection of the streamlines in the interaction region, is determined by integration of

$$U\frac{\partial y}{\partial x} + v\frac{\mathrm{d}Y}{\mathrm{d}z} = 0 \tag{13}$$

On the other hand, the temperature perturbation θ can be obtained from the condition of isentropic flow:

$$(\gamma-1)U\frac{\partial p}{\partial x} = \frac{U}{T}\frac{\partial \theta}{\partial x} + \frac{v}{T}\frac{\mathrm{d}T}{\mathrm{d}z} \tag{14}$$

or, more directly, from the linearized form of the equation of state

$$R\theta = \gamma p - T\rho - (W_2^{-1} - 1)RTy \tag{15}$$

in terms of ρ, p, and y.

As shown by Lighthill [19], Eq. (12) can be combined to produce a single equation for the pressure perturbation. The development uses suitable linear combinations of Eqs. (12a), (12b), and (12d) to yield

$$(1-M^2)\frac{\partial p}{\partial x} = \frac{\partial}{\partial z}\left(\frac{v}{U}\right) \tag{16}$$

which leads to

$$\frac{\partial^2 p}{\partial z^2} + (1-M^2)\frac{\partial^2 p}{\partial x^2} - \frac{\partial \ln M^2}{\partial z}\frac{\partial p}{\partial z} = 0 \tag{17}$$

after elimination of v, with use made of Eq. (12c). From Eq. (17), clearly, the solution depends fundamentally on the shape of the Mach number distribution $M(z)$.

Following Lighthill [19,20] , to simplify the treatment, we assume that the mixing layer extends across the finite domain $z_2 < z < z_1$ and that the base flow is uniform outside. The problem then reduces to that of integrating Eq. (17) in $z_2 < z < z_1$ subject to the condition that p decays as $x \to \pm\infty$ and to the additional boundary conditions at $z = z_1$ and $z = z_2$ obtained from matching with the pressure field in the uniform streams. There, M^2 is constant and the pressure-perturbation field obeys the Prandtl–Glauert equation $\partial^2 p/\partial z^2 + (1-M^2)\partial^2 p/\partial x^2 = 0$, which results in a hyperbolic or elliptic differential equation, depending on whether the Mach number is larger or smaller than unity, respectively.

In the supersonic stream, the pressure waves follow real characteristic paths $C_\pm = x \pm \beta_1 z =$ constant, where $\beta_1 = (M_1^2 - 1)^{1/2}$, with the two solutions having different specific domains of dependence and ranges of influence. The pressure wave in the supersonic zone can be represented by an incident (known) wave, described by $f_1(x + \beta_1 z)$, and a reflected (unknown) wave, described by $g_1(x - \beta_1 z)$, so that $p = f_1(x + \beta_1 z) + g_1(x - \beta_1 z)$. This outer pressure field is to be employed when defining the boundary condition at $z = z_1$, given in the following for the Fourier analysis in Eq. (24). By way of contrast, since Eq. (17) is elliptic for subsonic flows, the associated characteristic paths are complex, corresponding to constant values of $x \pm i\beta_2 z$ with $\beta_2 = (1 - M_2^2)^{1/2}$, causing the entire subsonic-flow domain to be the range of influence and domain of dependence. Boundedness of the solution as z approaches $-\infty$ then provides the additional needed boundary

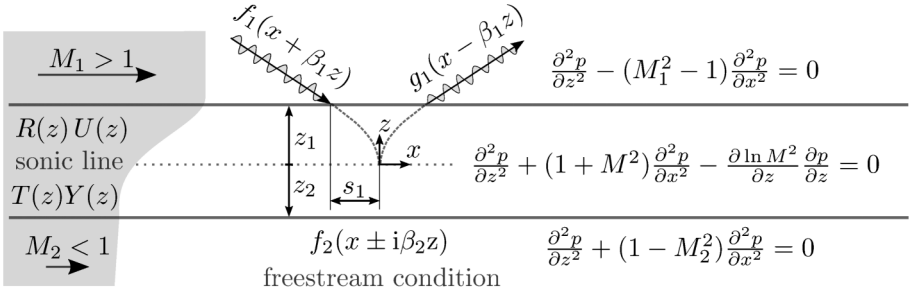

Fig. 4 Schematic representation of the incident wave mixing-layer interaction.

condition at $z = z_2$, given in Eq. (25) in Fourier space, thereby completing the definition of the pressure-perturbation problem.

The model of the interaction is sketched in Fig. 4, where the incident wave f_1 that travels along the path $x + \beta_1 z =$ constant interacts first with the mixing layer at $z = z_1$ and

$$x = -s_1 = -\int_0^{z_1} (M^2 - 1)^{1/2}\,\mathrm{d}z$$

The reflected wave g_1 leaves the mixing layer following the characteristic $x - \beta_1 z =$ constant. The functions $g_1(x - \beta_1 z)$ and $f_2(x \pm i\beta_2 z)$ are to be found by analyzing the interaction with the mixing layer for a given function $f_1(x + \beta_1 z)$.

C. Solution in Fourier Space

It is useful to transform the partial differential equation [Eq. (17)] into an ordinary differential equation for z by taking a Fourier transform over the x variable. The Fourier-transform pressure $\mathcal{P}(k, z)$ is defined by its inverse transform

$$p(x, z) = \frac{1}{\sqrt{2\pi}} \int_{-\infty}^{\infty} e^{ikx} \mathcal{P}(k, z)\,\mathrm{d}k \tag{18}$$

where the independent variable k refers to the Fourier wave number of the pressure disturbances. In the formalism selected here, the unitary transformation [Eq. (18)] includes a factor $1/\sqrt{2\pi}$ that is not present in Lighthill's boundary-layer analysis [19,20], which is a difference to be kept in mind when comparing the boundary-layer and mixing-layer results. In terms of $\mathcal{P}(k, z)$, the governing perturbation equation inside the mixing layer becomes

$$\frac{\mathrm{d}^2\mathcal{P}}{\mathrm{d}z^2} - \frac{\mathrm{d}\ln M^2}{\mathrm{d}z}\frac{\mathrm{d}\mathcal{P}}{\mathrm{d}z} + k^2(M^2 - 1)\mathcal{P} = 0 \tag{19}$$

Since M is constant in the supersonic and subsonic streams, in those streams, Eq. (19) reduces to the equation

$$\frac{\mathrm{d}^2\mathcal{P}}{\mathrm{d}z^2} + k^2(M^2 - 1)\mathcal{P} = 0 \tag{20}$$

The solutions to Eq. (20) are oscillatory in the supersonic stream ($M^2 > 1$) and exponential in the subsonic stream ($M^2 < 1$). In the former stream, the pressure field in Fourier space can be written as

$$\mathcal{P}(k, z) = F_1(k)e^{ik\beta_1 z} + G_1(k)e^{-ik\beta_1 z} \tag{21}$$

where $F_1(k)$ describes the incident perturbation, and $G_1(k)$ refers to the corresponding reflected wave. Since the incident perturbation must be prescribed for any given problem, the function $F_1(k)e^{ik\beta_1 z}$ is known. The function $G_1(k)$, however, is to be determined from Eq. (19) by satisfying the boundary condition in the subsonic stream as z approaches negative infinity. Since $G_1(k)$ is unknown, condition (21) must be replaced by a condition that does not involve $G_1(k)$. A suitable condition, evident from the derivative of Eq. (21), is

$$\frac{\mathrm{d}\mathcal{P}}{\mathrm{d}z} + i\beta_1 k\mathcal{P} = 2i\beta_1 k F_1(k)e^{ik\beta_1 z} \tag{22}$$

the right-hand side of which is now a prescribed function.

For any given value of k, Eq. (19) can be integrated numerically from a large positive value of z toward $z = -\infty$ if values of $F_1(k)$ and $G_1(k)$ are selected. At large negative values of z, this solution will approach the solution to the subsonic form of Eq. (20), which can be written as

$$\mathcal{P}(k, z) = F_2(k)e^{+|k|\beta_2 z} + G_2(k)e^{-|k|\beta_2 z} \tag{23}$$

with the values of $F_2(k)$ and $G_2(k)$ determined by the selected values of $F_1(k)$ and $G_1(k)$ through the integration of Eq. (19). Since the solution must, however, be bounded as z approaches negative infinity, $G_2(k)$ must vanish. Given $F_1(k)$, there will be a value of $G_1(k)$ that will result in $G_2(k) = 0$. This value of $G_1(k)$ will correspond to the correct value for the reflected wave. This shooting computational approach will provide $G_1(k)$ accurately because any inaccuracies in $G_1(k)$ would result in an exponentially divergent solution as z approaches negative infinity.

An alternative to this shooting method is to impose boundary conditions at sufficiently large but finite values of $|z|$, as did Lighthill [19]. If these boundaries are placed sufficiently far [i.e., at values of $|z|$ where Eq. (20) applies because the Mach number is close to its freestream values], then the solutions employing Eqs. (22) and (23) with $G_2(k) = 0$ at the computational boundaries will be sufficiently accurate. This approach, moreover, facilitates comparisons with the Lighthill solutions [19,20]. That approach is therefore selected here, with the values of z_1 and z_2 associated with the condition of achievement of 99% of the freestream Mach number, as previously mentioned.

Applying Eq. (22) at $z = z_1$ gives

$$\mathcal{P}_z(k, z_1) + i\beta_1 k\mathcal{P}(k, z_1) = 2i\beta_1 k F_1(k)e^{ik\beta_1 z_1} \tag{24}$$

where the subscript z denotes differentiation with respect to this coordinate. In the external subsonic zone, where the pressure distribution [Eq. (23)] holds, the function $G_2(k)$ must vanish to avoid a divergent behavior when $z \to -\infty$, as previously mentioned. Correspondingly, the boundary condition for $\mathcal{P}$ at $z = z_2$ becomes

$$\mathcal{P}_z(k, z_2) = \beta_2 |k| \mathcal{P}(k, z_2) \tag{25}$$

For a given $F_1(k)$, the pressure perturbation in the mixing layer $\mathcal{P}(k, z)$ is obtained by integrating Eq. (19) subject to Eqs. (24) and (25). The Fourier transform of the remaining flow variables can be written in terms of $\mathcal{P}$ and $\mathcal{P}_z$. For instance, the functions $\mathcal{Y}(k, z)$ and $\Theta(k, z)$, corresponding to $y(x, z)$ and $\theta(x, z)$ in Fourier space, can be evaluated from

$$\mathcal{Y} = -\frac{\mathrm{d}Y}{\mathrm{d}z}\frac{\mathcal{P}_z}{k^2 M^2} \tag{26}$$

and

$$\Theta = (\gamma - 1)T\mathcal{P} - \frac{\mathrm{d}T}{\mathrm{d}z}\frac{\mathcal{P}_z}{k^2M^2} \tag{27}$$

obtained from streamwise derivatives of Eqs. (13) and (14) after Eq. (12c) is used to express $\partial v/\partial x$ in terms of the transverse pressure gradient. Also, the solution for $\mathcal{P}(k,z)$ can be used to determine the pressure perturbations in the outer streams, including the reflected wave

$$G_1(k) = \frac{ik\beta_1\mathcal{P}(k,z_1) - \mathcal{P}_z(k,z_1)}{2ik\beta_1}e^{ik\beta_1 z_1} \tag{28}$$

in the supersonic stream, obtained by appropriately eliminating $F_1(k)$ after differentiating Eq. (21) and evaluating the result at $z = z_1$, as well as the transmitted pressure perturbations

$$F_2(k) = \mathcal{P}(k,z_2)e^{-|k|\beta_2 z_2} \tag{29}$$

in the subsonic stream, obtained by evaluating Eq. (23) at $z = z_2$ with $G_2 = 0$.

III. Formal Solution in Fourier Space and Limiting Asymptotic Forms

The problem of finding $\mathcal{P}(k,z)$ requires numerical integration. The small-scale and large-scale structures of the pressure field can be investigated by considering analytic solutions for large and small values of $|k|$, respectively. To facilitate the analytical development, it is convenient to express the solution formally in terms of two independent orthogonal functions, Q and N, defined by the solutions to Eq. (19) that obey the modified boundary conditions

$$\begin{aligned} Q(k,z_2) &= 1, \qquad & Q_z(k,z_2) &= 0 \\ N(k,z_2) &= 0, \qquad & N_z(k,z_2) &= 1 \end{aligned} \tag{30}$$

Using these two independent solutions together with the original boundary conditions [Eqs. (24) and (25)] enables the pressure $\mathcal{P}(k,z)$ to be expressed in the form

$$\frac{\mathcal{P}(k,z)}{F_1(k)} = \frac{2i\beta_1 k[Q(k,z) + \beta_2|k|N(k,z)]}{E(k,z_1,\beta_1,\beta_2)}e^{ik\beta_1 z_1} \tag{31}$$

with

$$E(k,z_1,\beta_1,\beta_2)$$

given by

$$\begin{aligned} E(k,z_1,\beta_1,\beta_2) &= Q_z(k,z_1) + i\beta_1 kQ(k,z_1) \\ &\quad + \beta_2|k|[N_z(k,z_1) + i\beta_1 kN(k,z_1)] \end{aligned} \tag{32}$$

In particular, Eq. (31) exhibits a linear dependence on the external perturbation $F_1(k)$ and a more complicated dependence on the Mach number distribution through the functions $Q(k,z)$ and $N(k,z)$. Solutions will be obtained in the following in the limit $|k| \gg 1$ by using the Wentzel–Kramers–Brillouin (WKB)-like method developed by Langer [33] and in the limit $|k| \ll 1$ by introducing regular expansions in powers of k^2 for $Q(k,z)$ and $N(k,z)$. The formal solution [Eq. (31)] is also useful to investigate the upstream influence of the pressure disturbance, for which the rate decays for $x \to -\infty$ as determined by the negative imaginary zero of the denominator of Eq. (31) with the smallest magnitude $|k|$. This aspect of the solution is to be investigated in Sec. V, including the differences with the boundary-layer results of Lighthill [19,20].

A. Limit of Large Wave Number

Consideration of the asymptotic limit of $k \gg 1$ allows us to explore the small-scale features of the flow. For the analysis, it is convenient to use, following [19], the early WKB-like results obtained by Langer [33] for equations of the form in Eq. (19). According to Langer's analysis, if the two variable coefficients $\mathrm{d}(\ln M^2)/\mathrm{d}\eta$ and (M^2-1) are twice differentiable in the interval $z_2 < z < z_1$, with the latter further satisfying $(M^2-1) > 0$ for $z > 0$ and $(M^2-1) < 0$ for $z < 0$, as is the case for the transonic mixing layer, then at the leading order in the limit $k \gg 1$, any solution to Eq. (19) can be expressed as a linear combination of the functions

$$\begin{aligned} f_a &= \sqrt{2\pi}M\frac{|s|^{1/6}}{|\beta|^{1/2}}(ks)^{1/3}J_{-1/3}(ks), \\ f_b &= \sqrt{2\pi}M\frac{|s|^{5/6}}{|\beta|^{1/2}}(ks)^{-1/3}J_{1/3}(ks)\mathrm{sign}(z) \end{aligned} \tag{33}$$

in which

$$\beta = (M^2-1)^{1/2}, \quad \text{and} \quad s = \int_0^z \beta(z')\,\mathrm{d}z' \tag{34}$$

with z' being a dummy integration variable and J_ν representing Bessel functions of the first kind. The stretched coordinate s is real in the supersonic domain $z > 0$ but imaginary for $z < 0$. Its value at $z = z_1$ is

$$s = s_1 = \int_0^{z_1} \beta(z)\,\mathrm{d}z$$

whereas that at the subsonic edge is given by $s = +is_2$, where

$$s_2 = \int_{z_2}^0 (1-M^2)^{1/2}\,\mathrm{d}z \tag{35}$$

Equations (33) simplify for values of s such that $|ks| \gg 1$, corresponding to any fixed transverse location z away from the sonic line as $|k| \to \infty$, in that the functions $(ks)^{\pm 1/3}J_{\mp 1/3}(ks)$ can be replaced by their asymptotic expressions for large values of the argument, leading to

$$\begin{aligned} f_a &= M\frac{|s|^{1/6}}{|\beta|^{1/2}}\left[\frac{e^{iks}}{(iks)^{1/6}} + \frac{e^{-iks}}{(-iks)^{1/6}}\right], \\ f_b &= M\frac{|s|^{5/6}}{|\beta|^{1/2}}\left[\frac{e^{iks}}{(iks)^{5/6}} + \frac{e^{-iks}}{(-iks)^{5/6}}\right]\mathrm{sign}(z) \end{aligned} \tag{36}$$

The constants of integration

$$C_a^Q(k) = \frac{1}{2\sqrt{3}}\frac{\sqrt{\beta_2}}{M_2}(k^{1/6}e^{ks_2} + (-k)^{1/6}e^{-ks_2}) \tag{37a}$$

$$C_b^Q(k) = \frac{1}{2\sqrt{3}}\frac{\sqrt{\beta_2}}{M_2}(k^{5/6}e^{ks_2} + (-k)^{5/6}e^{-ks_2}) \tag{37b}$$

$$C_a^N(k) = \frac{1}{2\sqrt{3}}\frac{1}{k\sqrt{\beta_2}M_2}(k^{1/6}e^{ks_2} - (-k)^{1/6}e^{-ks_2}) \tag{37c}$$

$$C_b^N(k) = \frac{1}{2\sqrt{3}}\frac{1}{k\sqrt{\beta_2}M_2}(k^{5/6}e^{ks_2} - (-k)^{5/6}e^{-ks_2}) \tag{37d}$$

that complete the determination of $Q = C_a^Q f_a + C_b^Q f_b$ and $N = C_a^N f_a + C_b^N f_b$ are obtained by imposing the boundary conditions [Eq. (30)] at the subsonic edge of the mixing layer, with the simplified expressions of Eq. (36) used in the evaluations, as is appropriate away from the sonic point. These simplified expressions can also be used to

evaluate the denominator of Eq. (31), which involves values of the functions and their derivatives at the supersonic edge of the mixing layer, whereas the complete expressions of Eq. (33) must be used for computing the functions Q and N appearing in the numerator, if a solution that is valid across the whole mixing layer is to be derived. This evaluation procedure provides

$$\frac{\mathcal{P}(k,z)}{F_1(k)} = \frac{M_2\sqrt{\beta_1}}{M_1\sqrt{\beta_2}}\frac{C_a^Q f_a + C_b^Q f_b + \beta_2|k|(C_a^N f_a + C_b^N f_b)}{k\cosh(ks_2 - i\pi/4) + |k|\sinh(ks_2 - i\pi/4)} k e^{ik(\beta_1 z_1 - s_1)} \tag{38}$$

as a uniformly valid expression for the transverse distribution of pressure perturbation for $k \gg 1$, giving, in particular,

$$\frac{\mathcal{P}(k,0)}{F_1(k)} = \frac{2^{1/3}\sqrt{\pi}}{3^{2/3}(-\frac{1}{3})!}\frac{\sqrt{\beta_1}}{M_1[M_z(0)]^{1/6}}[1 + i\,\mathrm{sign}(k)]|k|^{1/6} e^{ik(\beta_1 z_1 - s_1)} \tag{39}$$

for the corresponding variation of the pressure at the sonic line $z = 0$, which is seen to exhibit a weak dependence on the local Mach number gradient $M_z(0) = (\mathrm{d}M/\mathrm{d}z)|_{z=0}$.

Away from the sonic point (i.e., for z such that $|ks| \gg 1$), one may use Eq. (36) to evaluate f_a and f_b in Eq. (38), yielding the simplified expressions

$$\frac{\mathcal{P}(k,z)}{F_1(k)} = \sqrt{\frac{\beta_1}{\beta}}\frac{M}{M_1}[e^{iks} + i\mathrm{sign}(k)e^{-iks}]e^{ik(\beta_1 z_1 - s_1)} \tag{40}$$

for $z \gg |k|^{-1}$, where the pressure is oscillatory, and

$$\frac{\mathcal{P}(k,z)}{F_1(k)} = \sqrt{\frac{\beta_1}{2|\beta|}}\frac{M}{M_1}[1 + i\mathrm{sign}(k)]e^{-|k||s|}e^{ik(\beta_1 z_1 - s_1)} \tag{41}$$

for $-z \gg |k|^{-1}$, where the pressure decays exponentially for increasing distances from the sonic line. Correspondingly, the large wave number components of the reflected and transmitted waves can be obtained by substituting Eq. (40) into Eq. (28) to give

$$G_1(k) = i\mathrm{sign}(k)e^{2ik(\beta_1 z_1 - s_1)}F_1(k) \tag{42}$$

and Eq. (41) into Eq. (29) to give

$$F_2(k) = \sqrt{\frac{\beta_1}{2\beta_2}}\frac{M_2}{M_1}[1 + i\mathrm{sign}(k)]e^{|k|(\beta_2 z_2 - s_2)}e^{ik(\beta_1 z_1 - s_1)}F_1(k) \tag{43}$$

In consonance with Riley [23], the results at a leading order in the limit $|k| \gg 1$ indicate that the pressure distribution across the mixing layer resulting from the external perturbation becomes largely independent of the boundary condition at the lower edge. Correspondingly, the distribution of $\mathcal{P}$ across the mixing layer, given in Eq. (38) for $|k| \gg 1$, is identical to that computed by Lighthill [19,20] for a boundary-layer flow with the same Mach number distribution $M(z)$, except in a region of characteristic thickness $|k|^{-1}$ near the lower edge, where significant differences appear. As a result, although the pressure perturbation at the sonic line, given in Eq. (39), and the shape of the reflected wave, given in Eq. (42), are identical for a mixing layer and a boundary layer that have the same $M(z)$ in the supersonic domain, the corresponding pressure at the mixing-layer subsonic boundary, obtained by evaluating Eq. (41) at $z = z_2$, is half the value predicted by Lighthill at the boundary-layer wall, given by equation 23 in [20]. Clearly, these differences in pressure magnitude are associated with the different nature of the boundary, with the confinement exerted by the wall resulting in higher pressures.

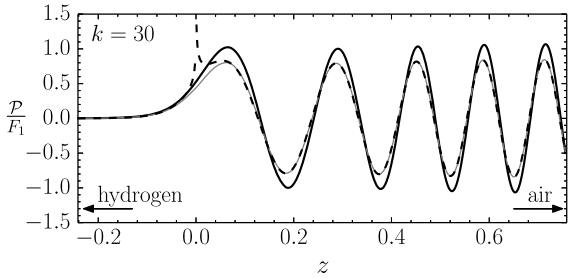

Fig. 5 Real part of $\mathcal{P}/F_1(k = 30)$ by computing Eq. (19) (thick, black, solid curves), Eq. (38) (thin, gray, solid curves) and in Eqs. (40) and (41) (dashed curves).

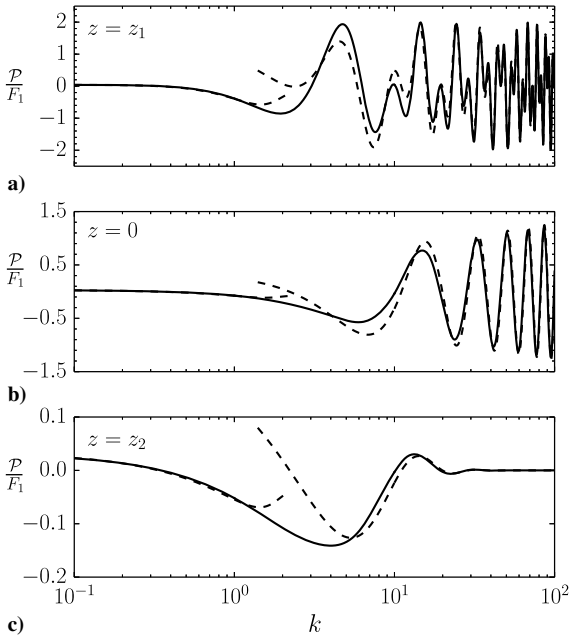

Fig. 6 Real part of the function $\mathcal{P}/F_1(k)$ at $z = z_1$ a), $z = 0$ b), and $z = z_2$ c), by computing Eq. (19) (solid curves) and the small and large limits (dashed curves).

The accuracy of the aforementioned large wave-number asymptotic predictions is tested in Fig. 5, which compares the variation with z of the real part of $\mathcal{P}/F_1$ obtained by numerical integration of Eq. (19) subject to Eqs. (24) and (25) with that evaluated with use made of Eq. (38) for the hydrogen–air mixing layer of Fig. 3d. For the value $k = 30$ selected, the differences are seen to be very small everywhere. The separate predictions given in Eqs. (40) and (41) for the pressure disturbances in the supersonic and subsonic domains are also included in the plot. As expected, these simplified expressions give a sufficiently accurate description away from the sonic point, but they break down as $M \to 1$ in the region where $|ks|$ is no longer small, where Eqs. (40) and (41) predict an erroneous pressure divergence resulting from the associated factors $1/\sqrt{\beta}$ and $1/\sqrt{|\beta|}$.

The asymptotic results are further tested in Figs. 6a–6c, which compare the variation with wave number of the real part of $\mathcal{P}/F_1$ at $z = (z_1, 0, z_2)$ obtained numerically with those determined from evaluations of the analytic predictions, given in Eq. (39) for the pressure at the sonic line $z = 0$ and in Eqs. (40) and (41) for the pressure at the supersonic and subsonic mixing-layer boundaries, respectively (results corresponding to the small wave-number limit, to be discussed in the following, are also included in the figure). As can be seen, at all three locations, the asymptotic predictions remain reasonably accurate until the wave number decreases to values of order unity.

The large wave-number predictions given previously can also be used to evaluate the perturbations to the other flow variables, e.g., those of the fuel mass fraction and temperature, given in Eqs. (26) and

(27). As expected, the deflection of the streamlines has a negligible influence on the large wave-number component of the solution so that, in the limit $|k| \gg 1$, the mass fraction perturbation $\mathcal{Y}$ vanishes, whereas the temperature perturbation [Eq. (27)] reduces to the local isentropic balance $\Theta/T = (\gamma - 1)\mathcal{P}$.

B. Limit of Small Wave Number

In the opposite limit $|k| \ll 1$, the solution can be obtained by introducing the expansions $Q(k, z) = Q_0(z) + k^2 Q_1(z) + \cdots$ and $N(k, z) = N_0(z) + k^2 N_1(z) + \cdots$ into Eq. (19) and solving sequentially the equations that appear at different orders in powers of k^2. The development is facilitated by writing Eq. (19) in the compact form

$$\frac{\mathrm{d}}{\mathrm{d}z}\left(M^{-2}\frac{\mathrm{d}\mathcal{P}}{\mathrm{d}z}\right) = k^2(M^{-2} - 1)\mathcal{P} \tag{44}$$

The right-hand-side term is absent in the equation at leading order

$$\frac{\mathrm{d}}{\mathrm{d}z}\left(M^{-2}\frac{\mathrm{d}\mathcal{P}_0}{\mathrm{d}z}\right) = 0 \tag{45}$$

where $\mathcal{P}_0$ is used to denote either one of the leading-order terms Q_0 and N_0 so that straightforward integration with boundary conditions $Q_0 - 1 = (Q_0)_z = 0$ and $N_0 = (N_0)_z - 1 = 0$ at $z = z_2$ provides

$$Q_0 = 1 \quad \text{and} \quad N_0 = \int_{z_2}^{z}\left(\frac{M}{M_2}\right)^2 \mathrm{d}z' \tag{46}$$

At the following order, we find

$$\frac{\mathrm{d}}{\mathrm{d}z}\left(M^{-2}\frac{\mathrm{d}\mathcal{P}_1}{\mathrm{d}z}\right) = k^2(M^{-2} - 1)\mathcal{P}_0 \tag{47}$$

thereby providing

$$Q_1 = \int_{z_2}^{z} M^2\left(\int_{z_2}^{z'}(M^{-2} - 1)\mathrm{d}z''\right)\mathrm{d}z' \tag{48}$$

and

$$N_1 = \int_{z_2}^{z} M^2\left(\int_{z_2}^{z'}(M^{-2} - 1)N_0\,\mathrm{d}z''\right)\mathrm{d}z' \tag{49}$$

upon integration with the homogeneous boundary conditions $Q_1 = (Q_1)_z = N_1 = (N_1)_z = 0$ at $z = z_2$.

Substitution of the resulting two-term expansions $Q(k, z) = Q_0(z) + k^2 Q_1(z)$ and $N(k, z) = N_0(z) + k^2 N_1(z)$ into Eq. (31) provides an explicit expression for the small wave-number pressure distribution that is accurate to order $O(k^2)$ across the mixing layer. The resulting prediction at $z = (z_1, 0, z_2)$ is compared with the complete numerical results in Figs. 6a–6c. As can be seen, the two-term expansion for $|k| \ll 1$ remains reasonably accurate for values of the wave number $|k| \leq 1$.

IV. Upstream Decay of the Disturbance

To investigate the upstream propagation of pressure disturbances on the subsonic side of the mixing layer, we adopt the solution strategy used by Lighthill [19] for the boundary layer. For $x < 0$, the inverse transform $p(x, z)$ of Eq. (18) can be expressed as $-\sqrt{2\pi}i$ times the sum of the residues of

$\mathcal{P}(k, z)e^{ikx}$ at the zeros of the denominator of Eq. (31) in the lower half of the complex k plane, which are located along the imaginary axis (i.e., $k = -i\kappa_0, -i\kappa_1, -i\kappa_2, \ldots$ with $\kappa_0 < \kappa_1 < \kappa_2 \cdots$). The dominant term in the far field, corresponding to large values of $-x$, is that associated with the smallest zero, $k = -i\kappa_0$. Correspondingly, the product of the inverse logarithmic decrement, κ_0^{-1}, and the mixing-layer thickness ℓ_m provides a measure for the effective distance of upstream influence.

To determine κ_0, it is convenient to introduce $k = -i\kappa$ in the denominator of Eq. (31) to yield

$$Q_z(-i\kappa, z_1) + \beta_1\kappa Q(-i\kappa, z_1) + \beta_2\kappa[N_z(-i\kappa, z_1) - \beta_1\kappa N(-i\kappa, z_1)] = E(-i\kappa, z_1, \beta_1, \beta_2) = 0 \tag{50}$$

where the functions Q and N are obtained by integration of Eq. (19) with the boundary conditions of Eq. (30). For a given Mach number distribution, the numerical solution to Eq. (50) provides a discrete number of real positive zeros κ_n of increasing magnitude. For instance, when the profiles $M(z)$ shown in Figs. 3c and 3d are used in the computation of $Q(k, z)$ and $N(k, z)$, one obtains for the first three zeros from Eq. (50) the values $\kappa_0 = 4.7$, $\kappa_1 = 16.34$, and $\kappa_2 = 27.23$ for the ethylene–air mixing layer and the values $\kappa_0 = 7.32$, $\kappa_1 = 27.6$, and $\kappa_2 = 45.22$ for the hydrogen–air mixing layer.

The results indicate that, for mixing layers, the decay of the perturbation is quite rapid because κ_0 is moderately large, so that the pressure disturbance is only felt at distances of the order of a fraction of the mixing-layer thickness. This is in contrast with the results previously obtained for the boundary layer, in which the decay was seen to be very slow [20], with perturbations reaching far upstream, but it agrees with the results of Riley [23]. Since κ_0 was very small for the boundary layer, the limit of small wave numbers was correspondingly used by Lighthill [20] to determine approximate analytic expressions for κ_0^{-1}. In the present problem, however, the numerical results suggest that the opposite limit $|k| \gg 1$ should be considered instead, with the value of κ_0 obtained from the analysis of the zeros of the denominator in Eq. (38), similar to what was done by Riley [23]. Introducing $k = -i\kappa$ leads to $\tan(\kappa s_2 + \pi/4) = -1$, which can be solved to give

$$\kappa_n = \frac{\pi}{2}(1 + 2n)s_2^{-1} \tag{51}$$

where s_2, defined in Eq. (35), carries a dependence on the Mach number distribution across the subsonic layer. Using in Eq. (51) the values $s_2 = 0.29$ and $s_2 = 0.175$ corresponding to the ethylene–air and hydrogen–air mixing layers, respectively, provides the values $\kappa_0 = 5.45$, $\kappa_1 = 16.34$, and $\kappa_2 = 27.23$; and $\kappa_0 = 8.98$, $\kappa_1 = 26.95$, and $\kappa_2 = 44.92$ for the first three zeros. As can be seen by comparing these values with the numerical results, the accuracy of Eq. (51) improves for larger κ, which is an expected result. The approximation $\kappa_0 = \pi/(2s_2)$ that follows from Eq. (51) overpredicts the first zero by about 20% for the two mixing layers considered here. As the Mach number of the subsonic stream decreases, the accuracies of these approximations decrease, approaching results like those of Lighthill [20].

It is worth mentioning that, although the inverse logarithmic decrement κ_0^{-1} in boundary layers is found to be approximately proportional to the square of the supersonic Mach number M_1^2 [20], in mixing layers, the large wave-number analysis provides a value $\kappa_0^{-1} = 2s_2/\pi$ entirely independent of the Mach number distribution in the supersonic stream. Since s_2 is proportional to $|z_2|$, the characteristic distance of upstream influence $\kappa_0^{-1}\ell_m$ becomes proportional to the thickness of the subsonic portion of the mixing layer, which is seen in Figs. 3c and 3d to be markedly smaller for the hydrogen–air mixing layer, as was indicated previously. The differences in profiles of $M(z)$ shown in Figs. 3c and 3d also indicate that consideration of a sufficiently accurate molecular-transport model is essential in computing s_2 accurately, so that, for instance, the Soret effects cannot be neglected when dealing with hydrogen.

V. Interaction with a Weak Shock

The aforementioned theory applies to the interaction of any given weak external pressure perturbation with a transonic mixing layer. The specific response to a weak shock can be investigated by considering an incident pressure jump defined by the Heaviside step function $f_1 = \mathcal{H}(x + \beta_1 z + s_1 - \beta_1 z_1)$, for which the Fourier transform is

given by $F_1(k) = (\pi\delta(k) + 1/ik)\exp[ik(s_1 - \beta_1 z_1)]/\sqrt{2\pi}$. The resulting distribution of pressure perturbation $p(x, z)$ across the mixing layer can be obtained from the inverse transformation [Eq. (18)] once the Fourier pressure function $\mathcal{P}(k, z)$ is determined by integration of Eq. (19) subject to Eqs. (24) and (25). Since the response to the pressure discontinuity is anticipated to have a dominant large wavenumber component at distances x of order unity, the simplified results obtained previously in the limit $|k| \gg 1$ can be used in the analysis of the solution in the interaction region. The computation of the pressure is still far from trivial, since it involves the cumbersome task of inverting the Bessel-type functions present in Eq. (38) when use is made of Eq. (33). The solution is facilitated by working with the simplified expressions [Eqs. (40) and (41)], which hold away from the sonic point in the supersonic and subsonic domains, respectively, yielding

$$p(x, z) = \sqrt{\frac{\beta_1}{\beta}}\frac{M}{M_1}\begin{cases}\mathcal{H}(x + s), & \text{if } x < s\\ -\tilde{\gamma}\pi^{-1} - \ln(x - s)\pi^{-1}, & \text{if } x > s\end{cases} \tag{52}$$

and

$$p(x, z) = \frac{1}{\pi}\sqrt{\frac{\beta_1}{2|\beta|}}\frac{M}{M_1}\left[\frac{\pi}{2} - \tilde{\gamma} - \ln\left(\sqrt{|s|^2 + x^2}\right) - \tan^{-1}\left(\frac{x}{|s|}\right)\right] \tag{53}$$

upon application of the inverse Fourier transform. The symbol $\tilde{\gamma}$ refers to the Euler–Mascheroni constant. These pressure functions are not valid in the vicinity of the sonic line $z = 0$, where they should be replaced by the inverse transform of the Fourier pressure [Eq. (38)]. In particular, its value at $z = 0$, given in Eq. (39), can be used to derive

$$p(x, 0) = \frac{\sqrt{\beta_1}}{\sqrt{2}M_1[M_z(0)]^{1/6}}\left[\frac{6^{1/3}(1/6)!\sqrt{2 + \sqrt{3}}}{(-1/3)!}\right] \times\left[1 + \frac{1 - (2 - \sqrt{3})\text{sign}(x)}{|x|^{1/6}}\right] \tag{54}$$

for the pressure perturbation along the sonic line.

The supersonic side pressure distribution [Eq. (52)] comprises two different waves, namely, the incident perturbation and a reflected wave. The former is just the incident step-pressure wave that follows the path $x = -s(z)$, with an amplitude proportional to $M/(M^2 - 1)^{1/4}$. On reflecting from the sonic line, the step changes its character to give a positive logarithmic infinity (i.e., a sudden compression followed by an expansion zone) that propagates outward along the characteristic $x = s(z)$. As the point of incidence $(x, z) = (0, 0)$ is approached, Eq. (52) ceases to be valid. The step and logarithmic singularities are seen to merge in the near-sonic region, leading to an algebraic singularity, with the pressure diverging proportional to $|M_z(0)x|^{-1/6}$, as can be seen in Eq. (54). In the subsonic layer, the solution given in Eq. (53) is regular for any nonzero value of $z < 0$. The solution is completed by the reflected wave in the outer supersonic zone:

$$g_1(x, z) = -\tilde{\gamma} - \frac{1}{\pi}\ln[x - \beta_1 z + \beta_1 z_1 - s_1] \tag{55}$$

which can be obtained directly by the Fourier inversion of Eq. (42) [or simply by setting $z = z_1$ in the right-traveling wave in Eq. (52)] and by the wave transmitted into the subsonic side:

$$f_2(x, z) = \frac{1}{\pi}\sqrt{\frac{\beta_1}{2\beta_2}}\frac{M_2}{M_1}\left\{\frac{\pi}{2} - \tilde{\gamma} - \tan^{-1}\left(\frac{x}{s_2 + \beta_2 z_2 - \beta_2 z}\right) - \ln\left[\sqrt{(s_2 + \beta_2 z_2 - \beta_2 z)^2 + x^2}\right]\right\} \tag{56}$$

obtained with use made of Eq. (53). Note that the logarithmic nature of g_1 corresponds to that of the mixing-layer pressure wave along the right-running characteristic $x = -s(z)$.

The pressure perturbations given in Eqs. (52) and (53) for the supersonic and subsonic domains and the intermediate sonic-line pressure distribution [Eq. (54)] are represented in Figs. 7a–7f for the ethylene–air and hydrogen–air mixing layers. The trajectories of the incident and reflected waves in the supersonic stream and the distributed pressure disturbances in the subsonic stream are qualitatively similar for both mixing layers, although quantitative differences arise from the associated differences in Mach number distribution displayed in Figs. 2c

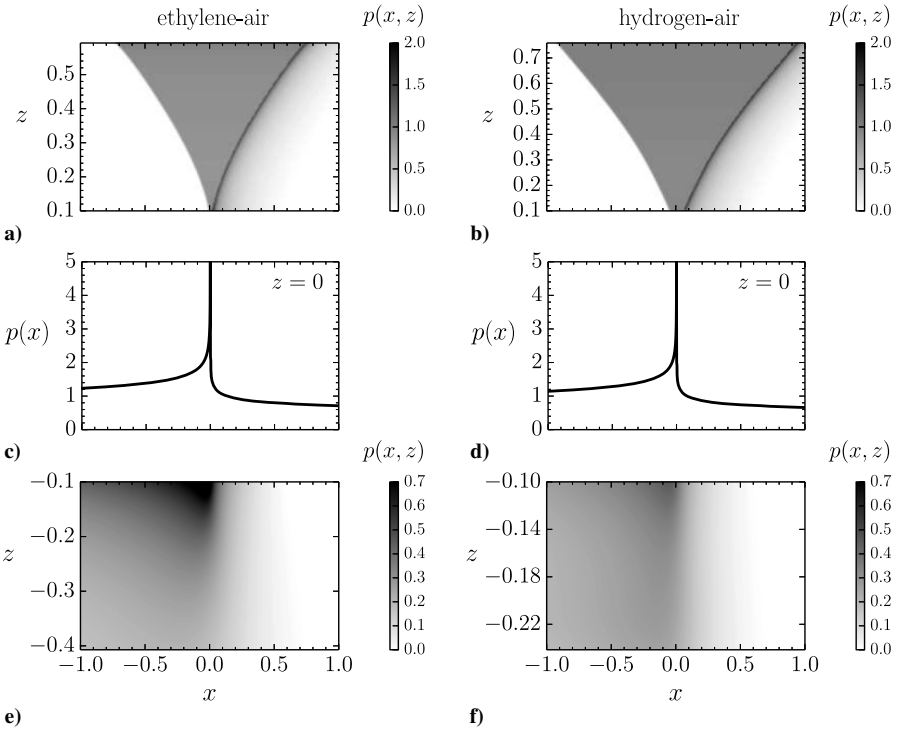

Fig. 7 Pressure perturbation from evaluation of Eq. (52) a, b), Eq. (54) c, d), and Eq. (53) e, f), for the ethylene–air (left-hand-side) and hydrogen–air (right-hand-side).

and 2d. Along the sonic line, however, the streamwise pressure distributions are practically indistinguishable because the values of $[M_z(0)]^{1/6}$ in Eq. (54) happen to be approximately equal for these two configurations. Since, in the limit of $|k| \gg 1$ the functions $\mathcal{P}$ and Θ are proportional, as dictated by Eq. (27), the corresponding temperature-perturbation field $\theta(x, z)$ would satisfy $\theta = (\gamma - 1)Tp$, thereby giving a spatial distribution qualitatively similar to that shown in Fig. 6 for the pressure-perturbation field.

The logarithmic singularity of the reflected wave and the algebraic singularity $|x|^{-1/6}$ at the point of incidence, both of which also are present in the original boundary-layer analysis of Lighthill [19], appear to be inconsistent with the hypothesis of small disturbances. They emerge in the linear theory as a consequence of the discontinuous nature of the incident pressure wave. It is naturally expected that, in realistic configurations, the singularity would disappear as a consequence of nonlinear effects acting locally, leading to a pressure field that would be similar to that depicted in Figs. 7a and 7f, except near the singularities, where the infinities would be replaced by large but finite values of the pressure. As noted by Lighthill [19] for boundary-layer flows, this view seems to be supported by experimental observations [34–37].

In the framework of the linear theory, the pressure singularity can be removed by accounting for the finite thickness of the incident weak shock: an approach that is motivated by the fact that the shock thickness is inversely proportional to the shock strength [38]. As a simplified example, one may consider external perturbations with a piecewise linear pressure distribution

$$f_1(x, z) = \frac{(x_+)\mathcal{H}(x_+) - (x_+ - \ell_s)\mathcal{H}(x_+ - \ell_s)}{\ell_s} \tag{57}$$

where $x_+ = x + \beta_1 z + s_1 - \beta_1 z_1$ is the incident wave path, and ℓ_s is the ratio of the shock-wave thickness to the mixing-layer thickness ℓ_m. The corresponding Fourier transform

$$F_1(k) = \left[\frac{1 - e^{ik\ell_s}}{k^2} + \ell_s \pi\delta(k)\right]\frac{e^{ik(s_1 - \beta_1 z_1)}}{\ell_s\sqrt{2\pi}} \tag{58}$$

can be used in the large wave-number prediction [Eq. (40)] to generate from Eq. (18) the pressure distribution

$$p(x, z) = \sqrt{\frac{\beta_1}{\beta}}\frac{M}{M_1}\left[\frac{(x+s)\mathcal{H}(x+s) - (x+s-\ell_s)\mathcal{H}(x+s-\ell_s)}{\ell_s}\right] \tag{59}$$

if $x < s$, and

$$p(x, z) = \sqrt{\frac{\beta_1}{\beta}}\frac{M}{M_1}\left[-\frac{\tilde{\gamma}+1}{\pi} - \frac{(x-s)\ln(x-s) - (x-s-\ell_s)\ln(x-s-\ell_s)}{\pi\ell_s}\right] \tag{60}$$

if $x > s$, which, unlike Eq. (52), yields a finite value of p along the right-running characteristic $x = -s(z)$. Similarly, contrary to their counterparts [Eq. (54) and (55)], the corresponding expressions for the pressure distribution along the sonic line

$$p(x, 0) = \frac{\sqrt{\beta_1}}{\sqrt{2}\ell_s M_1 [M_z(0)]^{1/6}}\frac{6^{1/3}(-5/6)!\sqrt{2+\sqrt{3}}}{5(-1/3)!} \times \left[(2-\sqrt{3})(|x-\ell_s|^{5/6} - |x|^{5/6}) - |x-\ell_s|^{5/6}\text{sign}(x-\ell_s) + |x|^{5/6}\text{sign}(x)\right] \tag{61}$$

and the associated reflected shock, which follows the path $x_- = x + \beta_1 z_1 - s_1 - \beta_1 z$,

$$g_1(x, z) = -\frac{\tilde{\gamma}+1}{\pi} - \frac{(x_-)\ln(x_-) - (x_- - \ell_s)\ln(x_- - \ell_s)}{\pi\ell_s} \tag{62}$$

are free from singularities, with the infinities in pressure present in Eqs. (54) and (55) being replaced by large peak values of order $\ell_s^{-1/6}$ in Eq. (61) and of order $\ln(\ell_s^{-1})$ in Eq. (62). These results indicate that the singularities of the infinitesimally thin shock translate into a ridge when the finite thickness of the shock is considered.

VI. Vorticity Production

Although, unlike the work of Buttsworth [25], only weak shocks are addressed in this study, the results can be used to examine trends of induced effects in applications involving shock wave ignition of fuel–air mixing-layer flows, which are of interest for combustion processes in supersonic engines. For example, the direct effects of the incident pressure wave on the fuel and temperature distributions are described by Eq. (26) and (27), giving results that could be incorporated as perturbations in computations of ignition distances by integration of the flow equations downstream from the interaction region. The results would be qualitatively indicative of the influences of stronger shocks.

The interaction of the pressure wave leads to an additional indirect (although possibly important) effect associated with the local generation of vorticity, which may promote the instability of the mixing-layer flow, thereby enhancing the combustion rate by increasing the downstream mixing rate of the two streams. Alternatively, this effect could also reduce the vorticity, and thereby inhibit instability and its associated turbulent mixing. In examining vorticity production, it is convenient to express the perturbed nondimensional vorticity, scaled with its characteristic value U_1'/ℓ_m, in the form $U_z(z) + \epsilon\omega(x, z)$. Here, U_z is clearly positive in the mixing layer and corresponds to a positive base-flow vorticity according to the conventional right-hand rule, with this being the component of the vorticity vector in the direction pointing into the paper (positive y direction in Fig. 2). Positive values of ω therefore increase the vorticity, and thus presumably enhance the instability of the laminar mixing layers, leading to an earlier onset of turbulence along with increased overall mixing rates.

The equation for $\omega = \partial u/\partial z - \partial v/\partial x$ can be shown from Eq. (12) to be given by

$$U\frac{\partial\omega}{\partial x} + vU_{zz} = U_z\left(\frac{\partial u}{\partial x} + \frac{\partial v}{\partial z}\right) - \frac{1}{M_1^2}\frac{R_z}{R^2}\frac{\partial p}{\partial x} \tag{63}$$

which indicates that, along the perturbed streamline, the vorticity changes through the combined effects of variable-density flow stretching and baroclinic torque: see the two source terms on the right-hand side of Eq. (63). The former arises as a result of the interaction of the induced dilatation rate with the background shear, whereas the latter is the result of the nonalignment of the induced pressure gradient and the background density gradient. The second term on the left-hand side of Eq. (63) emerges because of the deflection of the streamlines, with its magnitude being proportional to the curvature of the base-flow velocity U_{zz}.

The vorticity equation [Eq. (63)] can be expressed in a more compact form by using Eq. (1) together with

$$\frac{\partial u}{\partial x} + \frac{\partial v}{\partial z} = -U\frac{\partial p}{\partial x} \tag{64}$$

obtained from a straightforward combination of Eqs. (12a) and (12d) to yield

$$\frac{\partial\omega}{\partial x} = -\Omega\frac{\partial p}{\partial x} - \frac{U_{zz}}{U}v \tag{65}$$

where the vorticity-production factor

$$\Omega(z) = U_z + \frac{U}{M^2}\frac{R_z}{R} \tag{66}$$

measures the collective effects of flow stretching and baroclinic torque. Taking the streamwise derivative of Eq. (65) and expressing the result in Fourier space, after using Eq. (12c) to eliminate $\partial v/\partial x$, yields

$$\varpi = -\Omega\mathcal{P} - U_{zz}\frac{\mathcal{P}_z}{k^2M^2} \tag{67}$$

for the transform $\varpi(k, z)$ of the vorticity perturbation, defined by its inverse transform

$$\omega(x, z) = (2\pi)^{-1/2}\int_{-\infty}^{\infty} e^{ikx}\varpi(k, z)\,\mathrm{d}k \tag{68}$$

Equation (67) can be used to evaluate ϖ from the results of the pressure-perturbation transform $\mathcal{P}$ and its derivative $\mathcal{P}_z$, together with the transverse distributions of $\Omega(z)$, $U_{zz}(z)$, and $M(z)$. For large wave numbers $|k| \gg 1$, the streamline deflection is seen from Eq. (67) to produce a negligible influence, and the resulting vorticity field becomes linearly proportional to the pressure perturbation, with Ω entering as a proportionality factor.

Profiles of $\Omega(z)$ and its stretching and baroclinic contributions corresponding to the mixing layers of Figs. 2a and 2d are shown in Figs. 8a and 8b. For the hydrogen–air mixing layer, both U_z and R_z are positive, with the result that the flow stretching and baroclinic torque cooperate to create vorticity of the same sign. The resulting function Ω is everywhere positive and shows a prominent peak in the subsonic stream near the sonic line. For mixing layers with constant molecular weight approximating ethylene–air, however, $R_z < 0$, because the density is inversely proportional to the temperature and the airstream is hotter. In this case, the competition of flow stretching and baroclinic torque causes the resulting function Ω, shown in Fig. 8b, to be predominantly negative in the subsonic domain, where the baroclinic torque is dominant, and positive in the supersonic domain, where flow stretching prevails. Its magnitude is significantly smaller than that corresponding to hydrogen–air mixing layers, suggesting that the perturbations to the vorticity field are more important for the latter, especially in the vicinity of the sonic line. Clearly, many of these quantitative results depend on the specific set of boundary conditions selected for the mixing-layer problem. For example, consideration of smaller fuel-side temperatures T_2 is seen to extend the range of negative Ω in the ethylene–air mixing layer. Likewise, for sufficiently small T_2, a region of negative R_z appears in the hydrogen–air mixing layer near the subsonic boundary, where Ω may become negative.

According to Eq. (65), vorticity can be either created or destroyed depending on the sign of the product $-\Omega\partial p/\partial x$, with the U_{zz} term being smaller. This possibility of creation or destruction also occurs for finite-amplitude waves in purely supersonic flow [25]. It can be concluded from the pressure fields shown in Fig. 6 that, at any given transverse location z, there is an upstream region of adverse pressure gradient ($\partial p/\partial x > 0$), including a finite pressure jump across the shock in the supersonic stream and a downstream region of favorable pressure gradient ($\partial p/\partial x < 0$). For the hydrogen–air mixing-layer result in Fig. 7b, for which Ω is positive everywhere, vorticity is destroyed upstream and produced downstream all across the mixing layer. This interaction thus may tend to delay the transition to turbulence ahead of shock impingement in this case. For the other case considered, however, the sequence is reversed in the subsonic domain with $\Omega < 0$, where there is vorticity production in the upstream region of adverse pressure gradient followed by vorticity destruction in the downstream region with $\partial p/\partial x < 0$. The effect of the shock on mixing-layer transition will thus be different for different fuels and in different flows. These qualitative observations may be of help in attempts to tailor flows to affect mixing.

VII. Conclusions

A notable finding of this investigation is the relative simplicity of shock interaction with transonic mixing layers, in comparison with its interaction with boundary layers on walls, as studied by Lighthill [19,20]. The triple-deck analysis that underlies the latter problem reduces to just two decks for this mixing layer. The reason for this simplification is that the Mach number of the subsonic stream does not become small. The present analysis applies for a wide range of Mach numbers of order unity, but it fails if the subsonic-stream Mach number becomes small compared with unity.

Although the same generalized Prandtl–Glauert equation applies in the transonic region, a number of differences in conclusions arise from the fact that the appropriate asymptotic analyses for large Reynolds numbers in laminar flows differ in this transonic case. For example, although Lighthill [19,20] found that the pressure disturbances in the boundary layer made themselves felt far upstream from the point of shock wave impingement on the wall, in the transonic mixing layer, those influences were restricted to a small region, having a streamwise distance of the same order as the thickness of the mixing layer. As a consequence, in the context of the Fourier transform in the streamwise direction, the WKB asymptotic expansions for large values of the streamwise wave number provided more accurate results for variations of pressure-wave influences in the flow direction than did corresponding regular expansions for small values in transonic problems.

In this weak-shock limit, which decouples the underlying mixing-layer base flow from the pressure-interaction analysis, pressure-wave interactions modify the mixing layer appreciably, but only in a region extending upstream and downstream for a distance of the order of the mixing-layer thickness or less. It was found that an incident step-function pressure-wave curves and tends to become normal to the flow direction at the sonic line, with its discontinuity disappearing there but generating a distributed pressure field in the subsonic region. In addition, the sharp-fronted incident pressure wave generates a reflected wave that follows an approximately mirror-image trajectory in the supersonic stream but possesses a distributed rather than sharp structure, exhibiting a logarithmic profile that builds rapidly to pressures in excess of that of the incident wave but then slowly decays, reminiscent of a rarefaction. Even though the derived structures and wave dynamics pertain specifically to linear theory, similar behaviors would be expected for sufficiently weak finite-amplitude shocks, so long as their strength is not great enough to alter the incoming subsonic

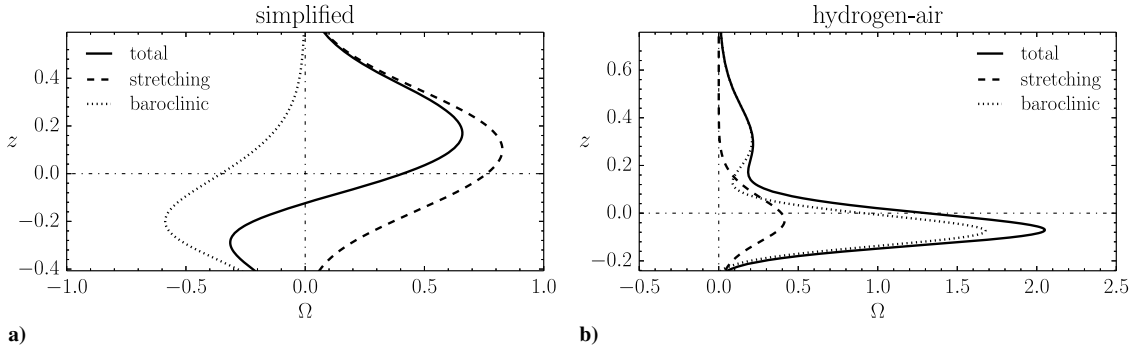

a) b)

Fig. 8 Vorticity-production factor Ω as a function of z for the ethylene–air (left-hand-side) and hydrogen–air mixing layers (right-hand-side).

portion of the mixing layer significantly. The methods of Riley [23] and Buttsworth [25] can address finite-amplitude influences in transonic and supersonic mixing layers, respectively.

Although these general attributes are common to all interactions of sufficiently weak pressure waves with transonic mixing layers, there are notable differences that depend on differences in the properties of ideal-gas mixtures that are assumed to be present in each of the two streams. The structures of the transonic mixing layers themselves differ, depending on the composition of each stream, even before any pressure-wave interaction. The two specific cases investigated here correspond to both streams effectively having the properties of air and to the supersonic stream being air and the subsonic-stream hydrogen. In the former case, more relevant for fuels such as ethylene, the transverse distribution across the mixing layer of the velocity, temperature, and composition variables are approximately symmetrical. In the latter case however, with hydrogen considered instead, the symmetry is broken, indicating the different behaviors of these two scramjet fuels.

The detailed consideration of the hydrogen case, motivated by interest in supersonic combustion, pertains to conditions in which the airstream is appreciably hotter than the hydrogen stream, as occurs in such applications. In that case, property variations across the mixing layer are asymmetrical. In particular the profile of the Mach number, which is of primary relevance to the pressure–wave interactions, although monotonic, nevertheless exhibits three points of inflection. Moreover, Soret diffusion exerts a strong influence on such profiles, whereas Dufour effects remain negligible. The presence of hydrogen also leads to an appreciably thicker mixing layer because of its large molecular diffusivity, with the sonic point occurring closer to the hydrogen side for a fixed Mach number ratio of the two streams because of its higher sound speed. These variations clearly depend strongly on the specific conditions selected for the analysis; and different profiles, in some cases even possibly nonmonotonic, would be encountered under other conditions.

The different structures of the mixing layers lead an incoming pressure wave to induce different modifications to those structures. For example, the modifications to the profiles of the temperature and composition fields are different in the two different cases analyzed. This will be significant in future considerations of influences of the incident waves on autoignition times in the mixing layers. Here, besides deriving the resulting temperature, pressure, and fuel-mass fraction fields, the different influences on modifications of vorticity profiles were examined, in particular, with the thought that increased vorticity enhances instabilities that result in transition to turbulence, which is beneficial to subsequent combustion, by introducing a turbulent contribution to the mixing.

Two physical phenomena were found to modify the vorticity fields, namely, the baroclinic torque produced by the pressure-gradient variation and the action of the local base-flow strain rate on the dilatation that is produced by the incident disturbance. A nondimensional function of the base-flow profiles was identified that quantifies the magnitude of the vorticity-field modifications, including both of these effects.

It was found that the incident perturbations could increase the vorticity in portions of the mixing layers and decrease it in other portions. For example, in the mixing layer with air properties on both sides, the relevant parameter is positive in the supersonic part of the mixing layer and negative in the subsonic part. The parameter was found to be positive everywhere across the mixing layer for the particular hydrogen case analyzed, although that need not be true always for hydrogen. It does, however, appear that, although the baroclinic and dilatation effects tend to be of opposite signs for mixing layers in which both streams have similar properties, they both tend to be positive with hydrogen in one stream, which is yet another difference for different scramjet fuels. Upstream from the impingement point, where the modifications to the vorticity generally are the largest, the effect is to reduce vorticity levels in the hydrogen–air mixing layer.

Ongoing extensions of this work include the consideration of nonlinear interactions of mixing layers with finite-amplitude shock waves that occur in scramjets [6,7,9–12]. In addition, particularly for the hydrogen–air case considered here, it is worthwhile to proceed to analyze the autoignition occurring in the laminar mixing layer to determine the extent to which pressure perturbations incident from the supersonic stream may augment ignition, thereby reducing ignition distances. Further extensions of this work also include consideration of shock-generated disturbances on steady combustion of diffusion flames. For all of these problems, turbulence is a complicating effect for which it could be misleading to try to extend the present results by simplified methods, such as merely replacing laminar diffusivities by turbulent diffusivities, since shock–turbulence interactions can be complex. Related problems for turbulent mixing layers therefore deserve extensive further study.

Acknowledgments

This work was supported by the U.S. Air Force Office of Scientific Research grants FA9550-12-1-0138 and FA9550-14-1-0219. We are grateful to Amable Liñán for useful conversations at the early stages of this project.

References

[1] Ferri, A., "Mixing-Controlled Supersonic Combustion," *Annual Review of Fluid Mechanics*, Vol. 5, No. 1, 1973, pp. 301–338. doi:10.1146/annurev.fl.05.010173.001505

[2] Andreopoulos, Y., Agui, J. H., and Briassulis, G., "Shock Wave-Turbulence Interactions," *Annual Review of Fluid Mechanics*, Vol. 32, No. 1, 2000, pp. 309–345. doi:10.1146/annurev.fluid.32.1.309

[3] Dolling, D. S., "Fifty Years of Shock-Wave/Boundary-Layer Interaction Research: What Next?," *AIAA Journal*, Vol. 39, No. 8, 2001, pp. 1517–1531. doi:10.2514/2.1476

[4] Jammalamadaka, A., Li, Z., and Jaberi, F., "Numerical Investigations of Shock Wave Interactions with a Supersonic Turbulent Boundary Layer," *Physics of Fluids*, Vol. 26, No. 5, 2014, Paper 056101. doi:10.1063/1.4873495

[5] Pirozzoli, S., and Bernardini, M., "Direct Numerical Simulation Database for Impinging Shock Wave/Turbulent Boundary-Layer Interaction," *AIAA Journal*, Vol. 49, No. 6, 2011, pp. 1307–1312. doi:10.2514/1.J050901

[6] Waidmann, W., Alff, F., Brummund, U., Böhm, M., Clauss, W., and Oschwald, M., "Experimental Investigation of the Combustion Process in a Supersonic Combustion Ramjet (SCRAMJET)," DLR Jahrestagung, DLR, German Aerospace Center, Erlangen, Germany 1994, pp. 629–638.

[7] Laurence, S. J., Karl, S., Schramm, J., Martnez, J., and Hannemann, K., "Transient Fluid-Combustion Phenomena in a Model Scramjet," *Journal of Fluid Mechanics*, Vol. 722, May 2013, pp. 85–120. doi:10.1017/jfm.2013.56

[8] Gutmark, E. J., Schadow, K. C., and Yu, K. H., "Mixing Enhancement in Supersonic Free Shear Flows," *Annual Review of Fluid Mechanics*, Vol. 27, No. 1, 1995, pp. 375–417. doi:10.1146/annurev.fl.27.010195.002111

[9] Menon, S., "Shock-Wave-Induced Mixing Enhancement in Scramjet Combustors," AIAA Paper 1989-0104, 1989.

[10] Lu, P. J., and Wu, K. C., "On the Shock Enhancement of Confined Supersonic Mixing Flows," *Physics of Fluids A*, Vol. 54, No. 12, 1991, pp. 3046–3062. doi:10.1063/1.857849

[11] Marble, F. E., "Gasdynamic Enhancement of Nonpremixed Combustion," *Proceedings of the Combustion Institute*, Vol. 25, No. 1, 1994, pp. 1–12. doi:10.1016/S0082-0784(06)80621-1

[12] Brummund, U., and Nuding, J. R., "Interaction of a Compressible Shear Layer with Shock Waves—An Experimental Study," AIAA Paper 1997-0392, 1997.

[13] Wepler, U., Huhn, Ch., and Koschel, W., "Numerical Simulation of Shock Wave Interaction Effects on Supersonic Mixing Layer Growth," *Numerical Flow Simulation II*, Vol. 75, Springer, New York, 2001, pp. 217–228. doi:10.1007/978-3-540-44567-8

[14] Zhang, Y., Wang, B., Zhang, H., and Xue, S., "Mixing Enhancement of Compressible Planar Mixing Layer Impinged by Oblique Shock Waves," *Journal of Propulsion and Power*, Vol. 31, No. 1, 2015, pp. 156–169. doi:10.2514/1.B35423

[15] Seiner, J. M., Dash, S. M., and Kenzakowski, D. C., "Historical Survey on Enhanced Mixing in Scramjet Engines," *Journal of Propulsion and*

Power, Vol. 17, No. 6, 2001, pp. 1273–1286.
doi:10.2514/2.5876

[16] Kim, J., Yoon, Y., Jeung, I., Huh, H., and Choi, J., "Numerical Study of Mixing Enhancement by Shock Waves in Model Scramjet Engine," *AIAA Journal*, Vol. 41, No. 6, 2003, pp. 1074–1080.
doi:10.2514/2.2047

[17] Génin, F., and Menon, S., "Studies of Shock/Turbulent Shear Layer Interaction Using Large-Eddy Simulation,"" *Computers and Fluids*, Vol. 39, No. 5, 2010, pp. 800–819.
doi:10.1016/j.compfluid.2009.12.008

[18] Kevlahan, N. K.-R., "The Propagation of Weak Shocks in Non-Uniform Flows," *Journal of Fluid Mechanics*, Vol. 327, Nov. 1996, pp. 161–197.
doi:10.1017/S0022112096008506

[19] Lighthill, M. J., "Reflection at a Laminar Boundary Layer of a Weak Steady Disturbance to a Supersonic Stream, Neglecting Viscosity and Heat Conduction," *Quarterly Journal of Mechanics and Applied Mathematics*, Vol. 54, No. 1, 1950, pp. 303–325.
doi:10.1093/qjmam/3.3.303

[20] Lighthill, M. J., "On Boundary Layers and Upstream Influence. II. Supersonic Flows Without Separation," *Proceedings of the Royal Society of London, Series A: Mathematical and Physical Sciences*, Vol. 217, No. 1131, May 1953, pp. 478–507.
doi:10.1098/rspa.1953.0075

[21] Stewartson, K., and Williams, P. G., "Self-Induced Separation," *Proceedings of the Royal Society of London, Series A: Mathematical and Physical Sciences*, Vol. 312, No. 1509, Sept. 1969, pp. 181–206.
doi:10.1098/rspa.1953.0075

[22] Nayfeh, A. H., "Triple-Deck Structure," *Computers Fluids*, Vol. 20, No. 1, 1991, pp. 269–292.
doi:10.1016/0045-7930(91)90044-I

[23] Riley, N., "Interaction of a Shock Wave with a Mixing Region," *Journal of Fluid Mechanics*, Vol. 7, No. 1, 1960, pp. 321–339.
doi:10.1017/S0022112060000116

[24] Moeckel, W. E., "Interaction of Oblique Shock Waves with Regions of Variable Pressure, Entropy, and Energy," NACA TN-2725, 1952, p. 35.

[25] Buttsworth, D. R., "Interaction of Oblique Shock Waves and Planar Mixing Regions," *Journal of Fluid Mechanics*, Vol. 306, No. 1, 1996, pp. 43–57.
doi:10.1017/S002211209600122X

[26] Dolvin, D., "Hypersonic International Flight Research and Experimentation (HiFiRE)," AIAA Paper 2008-2581, 1985.

[27] Muppala, S. P., Aluri, N. K., Dinkelacker, F., and Leipertz, A., "Development of an Algebraic Reaction Rate Closure for the Numerical Calculation of Turbulent Premixed Methane, Ethylene, and Propane/Air Flames for Pressures Up to 1.0 MPa," *Combustion and Flame*, Vol. 140, No. 4, 2005, pp. 257–266.
doi:10.1016/j.combustflame.2004.11.005

[28] Sánchez, A. L., and Williams, F. A., "Recent Advances in Understanding of Flammability Characteristics of Hydrogen," *Progress in Energy and Combustion Science*, Vol. 41, April 2014, pp.1–55.
doi:10.1016/j.pecs.2013.10.002

[29] Rosner, D. E., *Transport Processes in Chemically Reacting Flow Systems*, Courier Corp., North Chelmsford, MA, 2012, p. 109.

[30] Fernández-Tarrazo, E., Sánchez, A. L., and Williams, F. A., "Hydrogen-Air Mixing-Layer Ignition at Temperatures Below Crossover," *Combustion and Flame*, Vol. 160, No. 10, 2013, pp. 1981–1989.
doi:10.1016/j.combustflame.2013.04.027

[31] Lin, C. C., "On the Stability of the Laminar Mixing Region Between Two Parallel Streams in a Gas," NACA TN-2887, 1953.

[32] Papamoschou, P., and Roshko, A., "The Compressible Turbulent Shear Layer: An Experimental Study," *Journal of Fluid Mechanics*, Vol. 197, No. 1, 1988, pp. 453–477.
doi:10.1017/S0022112088003325

[33] Langer, R. E., "On the Asymptotic Solutions of Differential Equations, with an Application to the Bessel Functions of Large Complex Order," *Transactions of the American Mathematical Society*, Vol. 34, No. 1, 1932, pp. 447–447.
doi:10.1090/S0002-9947-1932-1501648-5

[34] Green, J. E., "Interactions Between Shock Waves and Turbulent Boundary Layers," *Progress in Aerospace Sciences*, Vol. 11, Dec. 1970, pp. 235–340.
doi:10.1016/0376-0421(70)90018-7

[35] Stalker, R. J., "Sweepback Effects in Turbulent Boundary-Layer Shock-Wave Interaction," *Journal of the Aerospace Sciences*, Vol. 27, No. 5, 1960, pp. 348–356.
doi:10.2514/8.8538

[36] Delery, J. M., "Experimental Investigation of Turbulence Properties in Transonic Shock Boundary-Layer Interactions," *AIAA Journal*, Vol. 21, No. 2, 1983, pp. 180–185.
doi:10.2514/3.8052

[37] Delery, J. M., "Shock Wave/Turbulent Boundary Layer Interaction and Its Control," *Progress in Aerospace Sciences*, Vol. 22, No. 4, 1985, pp. 209–280.
doi:10.1016/0376-0421(85)90001-6

[38] Zel'dovich, Y. B., and Raizer, Y. P., *Physics of Shock Waves and High-Temperature Hydrodynamic Phenomena*, Dover Publ., Mineola, NY, 2002, p. 80.

G. Blaisdell
Associate Editor